INTERNATIONAL JOURNAL FOR NUMERICAL METHODS IN FLUIDS
Int. J. Numer. Meth. Fluids 2004; **46**:1069–1098
Published online 27 September 2004 in Wiley InterScience (www.interscience.wiley.com). DOI: 10.1002/fld.783

Inviscid, laminar and turbulent opposed flows

Ersel Korusoy and J. H. Whitelaw*,†

Mechanical Engineering Department, Imperial College, London SW7 2BX, U.K.

SUMMARY

This paper attempts to reproduce numerically previous experimental findings with opposed flows and extends their range to quantify the effects of upstream pipes and nozzles with inviscid, laminar and turbulent flows. The choice of conservation equations, boundary conditions, algorithms for their solution, the degree of grid dependence, numerical diffusion and the validity of numerical approximations are justified with supporting calculations where necessary. The results of all calculations on the stagnation plane show maximum strain rates close to the annular exit from the nozzles and pipes for lower separations and it can be expected that corresponding reacting flows will tend to extinguish in this region with the extinction moving towards the axis. With laminar flows, the maximum strain rate increased with Reynolds number and the maximum values were generally greater than with inviscid flows and smaller than with turbulent flows. With large separations, the strain rates varied less and this explains some results with reacting flows where the extinction appeared to begin on the axis.

The turbulent-flow calculations allowed comparison of three common variants of a two-equation first-moment closure. They provided reasonable and useful indications of strain rates but none correctly represented the rms of velocity fluctuations on the axis and close to the stagnation plane. As expected, those designed to deal with this problem produced results in better agreement with experiment but were still imperfect. Copyright © 2004 John Wiley & Sons, Ltd.

KEY WORDS: opposed jets; strain rates; inviscid; laminar; turbulent; three two-equation models

1. INTRODUCTION

Opposed laminar and turbulent flows have been used to determine strain rates at extinction, for example References [1–6], and also provide a basis for the development of kinetic models of combustion, as by Hamins *et al.* [7], Fallon *et al.* [8], Gao *et al.* [9], Frouzakis *et al.* [10], Massot *et al.* [11], Sung *et al.* [12], Lahjaily *et al.* [13] and Zegers *et al.* [14]. Accurate determination of the isothermal flow field, including an assessment of turbulence modes, is essential prior to the added complexities of combustion and extinction and this motivated

*Correspondence to: J. H. Whitelaw, Mechanical Engineering Department, Imperial College, London SW7 2BX, U.K.
†E-mail: JHWhitelaw@compuserve.com

Contract/grant sponsor: United States Office of Naval Research; contract/grant number: N00014-99-1-0832 and N00014-02-1-0664

Received 21 January 2004
Revised 6 August 2004

many past contributions, for example numerical work with k–ε models including those in References [15–21] while some of the more recent work with Reynolds stress models includes the contributions of Champion and Libby [22, 23], Lindstedt and Váos [24]. The present calculations were guided in part by the previous work but mainly by the experiments of Korusoy and Whitelaw [25, 26]. The following three paragraphs review past work in inviscid, laminar and turbulent opposed flows followed by a consideration of the turbulence models used and the added complexity of combustion.

Early solutions of inviscid-flow equations, as by Leclerc [27] and included in the reviews of Spalding [28] and Tsuji [29], were based on the idealization of an infinite potential flow, where the magnitude of the axial component of velocity increased linearly with axial distance from the stagnation plane and the radial component increased linearly with radial distance from the axis of symmetry. The infinite potential flow field could be characterized by a single strain rate, given by the axial gradient of axial velocity at the stagnation point, and had the advantage that it reduced the conservation equations to a one-dimensional boundary value problem [10]. The utility of the infinite potential flow was limited since it did not conform to the wall boundary conditions at the exit planes of real geometries with finite separations and exit widths and Reference [30] proposed 'plug flow' boundary conditions, where uniform axial velocity and zero radial velocity were assumed at the nozzle exits. The present inviscid results provide a more complete pattern of results including profiles of strain rate.

Measurements of axial velocities in laminar flows with a laser-Doppler-anemometer [1] showed that they were closer to one-dimensional numerical calculations with plug flow boundary conditions than with the infinite potential flow. A simple empirical expression for the strain rate at the stagnation plane, based on numerical simulations with plug flow boundary conditions, was then proposed in terms of the bulk velocities and nozzle separation ($2U_b/H$ for symmetric nozzles and often called the bulk strain rate) and this was used in a wide range of opposed flows ranging from inviscid to turbulent. Limitations of the plug flow boundary conditions with nozzles at smaller separations were noted in laminar flows and numerical calculations of velocity along the axis overestimated measured values by a factor of slightly less than two. Planar visualizations of the laminar velocity field between opposed nozzles with 1.0 D separation [31] implied a minimum at the axis in the exit plane, with peaks away from it. Experiments with opposed pipes and laminar flows [3, 14] with separations of 2.0 and 1.0 D, respectively, also showed a change in the exit velocity profile at the smaller separation. The boundary layer thickness and the axial velocity at the centre of the exit plane were reduced, resulting in overestimated strain rates at the stagnation point.

With turbulent opposed flows, measured strain rates at the stagnation point [32] were lower than expected from the one-dimensional numerical calculations of [1] with plug flow boundary conditions, and this led to a modified empirical version of the bulk strain rate formula [33]. These findings may be linked to those of Gao *et al.* [9] and Massot *et al.* [11] that quantitative agreement between one-dimensional models and measurements required exit-plane boundary conditions and Frouzakis *et al.* [10] reported that one-dimensional calculations agreed with two-dimensional solutions only for separations of at least 1.0 D. The measurements of Rolon *et al.* [31] were extended in Reference [25] to demonstrate a peak in the profile of static pressure at the axis responsible for the minimum in the exit velocity, and consequent peaks in the profiles of strain rate at the stagnation plane of opposed nozzles with separations of 1.0 D or less and, in a subsequent contribution, the importance of local strain rates for local quenching and extinction was highlighted [26].

There are many turbulence models, see for example Reference [34], and it is clear that increasing complexity implies added cost. The simplest and cheapest are the one-equation mixing length models that have been very successful in the prediction of two-dimensional turbulent flows, e.g. see References [35, 36] and the review by Rodi [37], but it is well known that these models are limited since they take no account of transport of turbulence. Two-equation models such as that based on the transport of turbulent kinetic energy and dissipation rate overcome this limitation but the Boussinesq approximation remains, together with the assumption of gradient diffusive transport of k and ε, and calculations in a similar impinging jet geometry, with a wall-to-pipe separation of two diameters by Dianat *et al.* [18] showed that the k–ε model of Jones and Launder [15] tended to over-predict the turbulence intensity along the stagnation streamline by up to a factor of 4. The calculations of Craft *et al.* [17] used the k–ε model of Jones and Launder [15] to show that the turbulence intensities of Cooper *et al.* [38] were over-predicted by a factor of 6 along the impingement region adjacent to the wall when the wall-to-pipe separation was two diameters. The inaccuracies of the k–ε model were attributed to the inadequacy of the linear stress–strain relationship in regions of flow stagnation and curvature and this was supported by further calculations by Craft *et al.* [39] using an alternative non-linear cubic constitutive relation between Reynolds stress and strain rate that reproduced measured turbulence intensities across the impingement region to within 30%. In contrast to the findings in impinging flows, Reference [19] showed that the Jones and Launder model was able to reproduce distributions of the axial component of rms velocity along the stagnation streamline of opposed pipe flows to within 10% of the measurements of Mastorakos [4] with a separation 0.8 D. Jones [40] suggested the different findings in impinging and opposed flows was likely to be a consequence of the different boundary conditions at the stagnation plane.

The limitations of the Boussinesq assumption may be overcome, at least in part, by solving six separate equations for the transport of Reynolds stresses, as in Reference [18], where a second-moment Reynolds stress and first-moment k–ε models showed that the former reproduced measured distributions of rms velocity fluctuations along the axis of opposed flows to within 5%, much better than the factor of 4 overestimate reported with the first-moment closure. Similar comparisons in Reference [17] showed that agreement with measurements was within 15% along the impingement region adjacent to the wall and, again, far better than with their first-moment model. The second-moment calculations of Korusoy and Whitelaw [25] reproduced rms velocity fluctuations measured along the axis of opposed jets by Mastorakos [4] to within 10% showing that this was equivalent to the accuracy achieved with first-moment equations [19].

The difficulties presented by turbulent combustion models were reviewed in References [41, 42] and were evident in the series of paper [43–46] and in Reference [24]. These authors showed that finite step chemistry of a limited number of chemical species had to be assumed as an approximation to reduce computational cost, often with the consequence that extinction was not adequately represented. It was also evident that combustion implied further complications for the associated aerodynamic calculations that had to be capable of representing the effects of density fluctuations and it was argued that Reynolds stress transport assumptions involving gradient diffusion were inadequate in reacting flows. Reference [41] highlighted the importance of additional source terms in the turbulence equations to describe flame-generated turbulence, for example due to perpendicular pressure and density gradients.

A commercial code and a desktop computer were used here to determine the extent to which numerical solutions of two-dimensional forms of the equations representing conservation of mass and momentum can reproduce the isothermal-flow measurements of Korusoy and Whitelaw [25]. Numerical experiments were performed to determine the influence of distributions of nodes, and subsequently to quantify pressures and velocities in the exit planes of the two jets with boundary conditions assumed upstream and to determine the consequences of the assumption. The effect of upstream boundary conditions on profiles of strain rate at the stagnation plane was determined, including those appropriate to pipes and nozzles with inviscid, laminar or turbulent flows over a range of separations. Thus, the inviscid plug flow model was generalized to determine the extent to which an inlet boundary condition applied a finite distance upstream of the jet exit was able to describe non-uniformities downstream with comparisons to the laminar flow calculations. Turbulent flow calculations were compared with the measurements to determine the consequences of pipes and nozzles for strain rates and the relative merits of the turbulence models of Jones and Launder [15], Chen and Kim [47] and Yakhot *et al.* [48]. The first-moment models were chosen because of their low cost and widespread use in past literature and to provide a basis for future studies with second-moment closures and combustion and their application to the determination of strain rates as a function of separation is new.

The equations and boundary conditions necessary for their solution together with the numerical procedures used are stated in the following two sections. Section 3 considers the relationship between the grid and numerical diffusion and results are presented and discussed in Section 4. The paper ends with summary conclusions and recommendations for further work.

2. EQUATIONS AND BOUNDARY CONDITIONS

2.1. Continuity and transport

In steady two-dimensional isothermal and inviscid flows, the coefficients of viscosity are zero and there is no turbulence so that all components of the stress tensor are zero. Thus, the time-averaged equations without buoyancy or compressibility are

Continuity for all incompressible flows:

$$\frac{V}{r} + \frac{\partial V}{\partial r} + \frac{\partial U}{\partial z} = 0 \tag{1}$$

Transport of r component of momentum for inviscid flow:

$$-\frac{1}{\rho}\frac{\partial P}{\partial r} = \frac{V^2}{r} + V\frac{\partial V}{\partial r} + U\frac{\partial V}{\partial z} \tag{2}$$

Transport of z component of momentum for inviscid flow:

$$-\frac{1}{\rho}\frac{\partial P}{\partial z} = \frac{UV}{r} + V\frac{\partial U}{\partial r} + U\frac{\partial U}{\partial z} \tag{3}$$

where the cylindrical polar co-ordinate system is defined in Figure 1(a) with z the perpendicular distance from the stagnation plane, r the radial distance from the axis of symmetry,

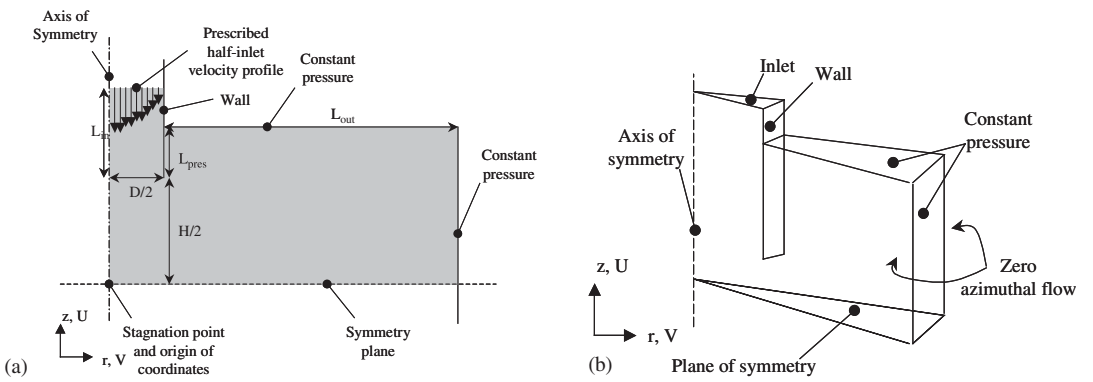

Figure 1. (a) Orientation and origin of the cylindrical polar co-ordinate system, dimensions of solution domain (shaded) and boundary conditions; and (b) finite volume representation of the solution domain.

U the mean axial velocity away from the stagnation plane and V is the mean radial velocity away from the axis.

Laminar flows have the same continuity equation but additional viscous stress terms mean the momentum conservation equations become

Transport of r component of momentum for laminar flow:

$$-\frac{1}{\rho}\frac{\partial P}{\partial r}+\frac{\mu}{\rho}\left(-\frac{V}{r^2}+\frac{1}{r}\frac{\partial V}{\partial r}+\frac{\partial^2 V}{\partial r^2}+\frac{\partial^2 V}{\partial z^2}\right)=\frac{V^2}{r}+V\frac{\partial V}{\partial r}+U\frac{\partial V}{\partial z} \tag{4}$$

Transport of z component of momentum for laminar flow:

$$-\frac{1}{\rho}\frac{\partial P}{\partial z}+\frac{\mu}{\rho}\left(\frac{1}{r}\frac{\partial U}{\partial r}+\frac{\partial^2 U}{\partial r^2}+\frac{\partial^2 U}{\partial z^2}\right)=\frac{UV}{r}+V\frac{\partial U}{\partial r}+U\frac{\partial U}{\partial z} \tag{5}$$

with the same assumptions of time averaging, no compressibility or buoyancy and the same cylindrical co-ordinate system.

The k–ε models used here for turbulent flows involved the well-known Boussinesq approximation that the Reynolds stress tensor is directly proportional to the strain rate tensor with the constant of proportionality equal to the eddy viscosity, as discussed by Jones and Whitelaw [15] who pointed out its shortcomings in regions of flow curvature or stagnation where turbulence is anisotropic and stated that such models should be used with the caveat that a loss of accuracy may occur.

Thus, the continuity equation is again unaltered and the momentum conservation equations become

Transport of r component of momentum for turbulent flow:

$$-\frac{1}{\rho}\frac{\partial P}{\partial r}+\frac{(\mu+\mu_t)}{\rho}\left(-\frac{V}{r^2}+\frac{1}{r}\frac{\partial V}{\partial r}+\frac{\partial^2 V}{\partial r^2}+\frac{\partial^2 V}{\partial z^2}\right)=\frac{V^2}{r}+V\frac{\partial V}{\partial r}+U\frac{\partial V}{\partial z} \tag{6}$$

Transport of z component of momentum for turbulent flow:

$$-\frac{1}{\rho}\frac{\partial P}{\partial z}+\frac{(\mu+\mu_t)}{\rho}\left(\frac{1}{r}\frac{\partial U}{\partial r}+\frac{\partial^2 U}{\partial r^2}+\frac{\partial^2 U}{\partial z^2}\right)=\frac{UV}{r}+V\frac{\partial U}{\partial r}+U\frac{\partial U}{\partial z} \tag{7}$$

Table I. Constants for Jones and Launder model.

C_μ	σ_k	σ_ε	$C_{\varepsilon 1}$	$C_{\varepsilon 2}$	K
0.090	1.000	1.300	2.000	1.550	0.410

Table II. Constants for Chen and Kim model.

C_μ	σ_k	σ_ε	$C_{\varepsilon 1}$	$C_{\varepsilon 2}$	K
0.090	0.750	1.150	1.900	1.150	0.415

Table III. Constants for renormalization group model.

C_μ	σ_k	σ_ε	$C_{\varepsilon 1}$	$C_{\varepsilon 2}$	K	n_0	β
0.085	0.719	0.719	1.680	1.420	0.400	4.380	0.012

where the eddy-viscosity, μ_t, can be determined from physical and dimensional arguments as

$$\mu_t = C_\mu \frac{\rho k^2}{\varepsilon} \tag{8}$$

with values for the constant, C_μ, as suggested by the authors of the models and listed for reference in Tables I–III. It should be noted that Equation (8) assumes the rates of production and dissipation of turbulence are at equilibrium and, as with the Boussinesq relation, this is incorrect in regions of flow curvature or stagnation adding to the possibility of inaccuracies.

2.2. *The Jones and Launder* [15] *model*

This k–ε model is the most common in general literature and has been developed extensively to include the effects of buoyancy, as in Reference [42] and compressibility, as in Reference [49]. It has been described by many authors and has come to be regarded as a 'standard' first-moment closure, as noted in Reference [17]. Thus, the transport and production equation for turbulent kinetic energy using the same cylindrical polar co-ordinate system in a steady incompressible flow is

Transport equation for k:

$$\rho\left(V\frac{\partial k}{\partial r} + U\frac{\partial k}{\partial z}\right) = \left(\frac{1}{r} + \frac{\partial}{\partial r}\right)\left(\mu + \frac{\mu_t}{\sigma_k}\right)\frac{\partial k}{\partial r} + \frac{\partial}{\partial z}\left(\mu + \frac{\mu_t}{\sigma_k}\right)\frac{\partial k}{\partial z} - \rho\varepsilon + 2\mu_t S_{ij}S_{ij} \tag{9}$$

where

$$S_{ij}S_{ij} = \left(\frac{V}{r}\right)^2 + \left(\frac{\partial V}{\partial r}\right)^2 + \left(\frac{\partial U}{\partial z}\right)^2 + \frac{1}{2}\left(\frac{\partial U}{\partial r} + \frac{\partial V}{\partial z}\right)^2$$

and the shorthand Cartesian notation $S_{ij}S_{ij}$ will be used in place of the explicit expression above for the remainder of this text. The term on the left-hand side of Equation (9) describes the convective transport of k while the first two terms on the right-hand side represent its gradient diffusion and the diffusivity of turbulent energy is related to the turbulent viscosity

by the dimensionless empirical number σ_k in Table I. The last two terms on the right-hand side of Equation (9) represent viscous dissipation of turbulent energy and its generation by shear stresses, respectively.

Finally, closure is achieved with the transport equation for viscous dissipation,

Transport equation for ε, *Jones and Launder model*:

$$\rho\left(V\frac{\partial\varepsilon}{\partial r}+U\frac{\partial\varepsilon}{\partial z}\right)=\left(\frac{1}{r}+\frac{\partial}{\partial r}\right)\left(\mu+\frac{\mu_t}{\sigma_k}\right)\frac{\partial\varepsilon}{\partial r}+\frac{\partial}{\partial z}\left(\mu+\frac{\mu_t}{\sigma_\varepsilon}\right)\frac{\partial\varepsilon}{\partial z}$$
$$-C_{\varepsilon1}\rho\frac{\varepsilon^2}{k}+2C_{\varepsilon2}\frac{\varepsilon}{k}\mu_t S_{ij}S_{ij} \tag{10}$$

where the term on the left-hand side and the first two terms on the right-hand side of Equation (10) are analogous to the k transport equation and represent convective and diffusive transport of dissipation, this time with the dimensionless empirical number σ_ε, Table I. The last two terms on the right-hand side of Equation (10) represent the destruction and production of ε and are directly proportional to the two terms on the right-hand side of Equation (9), describing destruction and production of k, where a factor of ε/k has been included to ensure dimensional consistency. The physical basis for the assumed proportionality comes from the condition that turbulent energy can never be negative or diverge, so the rate of energy dissipation must be similar to the rate of production together with the condition $\sigma_k<\sigma_\varepsilon$ and the two proportionality constants, $C_{\varepsilon1}$ and $C_{\varepsilon2}$, are given in Table I.

It is known that the Jones and Launder model generally leads to overestimates of the rms velocity fluctuations in regions of stagnation, for example Reference [18] showed that the rms was a factor of up to four times greater than measurements along the stagnation streamline of an impinging jet, and this implies the rate of production of ε is greater than that suggested by the last term on the right-hand side of Equation (10). This has led to a number of proposed modifications to the ε equation and two of the more common versions are described in the following two subsections.

2.2.1. The Chen and Kim [*47*] *model.* This model was devised to improve accuracy in predicting stagnating flows with the justification that an additional production timescale might be used to allow the energy transfer mechanism of turbulence to respond to the mean strain rate more effectively. This leads to the modified ε equation

Modified ε *equation of Chen and Kim*:

$$\rho\left(V\frac{\partial\varepsilon}{\partial r}+U\frac{\partial\varepsilon}{\partial z}\right)=\left(\frac{1}{r}+\frac{\partial}{\partial r}\right)\left(\mu+\frac{\mu_t}{\sigma_k}\right)\frac{\partial\varepsilon}{\partial r}+\frac{\partial}{\partial z}\left(\mu+\frac{\mu_t}{\sigma_\varepsilon}\right)\frac{\partial\varepsilon}{\partial z}$$
$$-C_{\varepsilon1}\rho\frac{\varepsilon^2}{k}+2C_{\varepsilon2}\frac{\varepsilon}{k}\mu_t S_{ij}S_{ij}+\frac{\mu_t^2}{\rho k}(S_{ij}S_{ij})^2 \tag{11}$$

where the values of the empirical coefficients, $C_{\varepsilon1}$ and $C_{\varepsilon2}$, proposed by Chen and Kim to give the best fit to data are given in Table II. The last term on the right-hand side of Equation (11) is new, contains the production timescale and marks the difference between the Chen and Kim and the Jones and Launder model.

2.2.2. The renormalization group (RNG) model. Yakhot and Orszag [48] suggested renormalization group analysis was a more rigorous and fundamental approach to the k–ε equations than the derivations outlined above and showed that a set of values for the coefficients may be determined analytically. The model implemented here conformed to that of Yakhot *et al.* [50] where the k equation was the same as that by Jones and Launder, but the ε equation was modified by an additional term that attempts to represent the increase in ε in regions of flow curvature or stagnation. Thus, the modified ε equation is

Modified ε equation of Yakhot et al.

$$\rho\left(V\frac{\partial\varepsilon}{\partial r}+U\frac{\partial\varepsilon}{\partial z}\right)=\left(\frac{1}{r}+\frac{\partial}{\partial r}\right)\left(\mu+\frac{\mu_t}{\sigma_k}\right)\frac{\partial\varepsilon}{\partial r}+\frac{\partial}{\partial z}\left(\mu+\frac{\mu_t}{\sigma_\varepsilon}\right)\frac{\partial\varepsilon}{\partial z}$$
$$-C_{\varepsilon1}\rho\frac{\varepsilon^2}{k}+2C_{\varepsilon2}\frac{\varepsilon}{k}\mu_t S_{ij}S_{ij}-C_\mu\frac{n^3(1-n/n_0)}{1+\beta n^3}\frac{\rho\varepsilon^2}{k} \tag{12}$$

where $n\equiv(k/\varepsilon)\sqrt{2S_{ij}S_{ij}}$. Values for the empirical coefficients n_0 and β were suggested and are given in Table III, together with the analytically derived values of the remaining coefficients. The difference between the RNG and Jones and Launder models is given by the additional last term on the right-hand side of Equation (12).

2.3. Boundary conditions

Figure 1 indicates the six types of boundary conditions, namely inlet, wall, symmetry plane, constant pressure, symmetry axis and zero azimuthal flow, and the position of the boundaries. A uniform inlet velocity profile equal to the bulk velocity was assumed for all inviscid flows while those with finite viscosity had to satisfy the zero slip condition at the point between the inlet and wall boundaries and, in turbulent flows, the well-known log-law of the wall was used.

Thus, in laminar nozzle flows that were undeveloped the inlet velocity profile increased sharply from zero at the wall to the bulk value one node away from it while a fully developed parabolic profile, $U=2(r^2/R^2-1)U_\mathrm{b}$, was used for laminar pipe flow. In turbulent nozzle flows, provision was made within the computational procedure so that the grid node neighbouring the wall was within the range $30<y^+<500$ where $y^+=\rho u_t y/\mu$ and $u_t=(\tau_w/\rho)^{1/2}$ and τ_w is wall shear stress. In terms of the dimensionless parameter $u^+=u/u_t$, the velocity profile in the region next to the wall, $y^+\leqslant y_m^+$, was assumed to be $u^+=y^+$ and the profile was $u^+=\mathrm{Ln}(9y^+)/K$ in the region $y^+>y_m^+$, and the value of y_m^+ was chosen to satisfy the relation $y_m^+=\mathrm{Ln}(9y_m^+)/K$ to prevent any discontinuities. The value of k at grid nodes neighbouring the wall was obtained from the transport equation while the dissipation was set to its equilibrium value, $\varepsilon=u_t^3/Ky$, in order to prevent divergence that otherwise occurred. Away from the first grid node and towards the axis of the inlet the velocity increased sharply to the bulk value in the case of turbulent nozzle flow, while it followed the seventh power law $U=9(r^7/R^7-1)U_\mathrm{b}/8$ for fully developed turbulent pipe flows. In all cases, inlet values of turbulence intensity and length scale were set to 12% and 4 mm in accordance with past measurements.

The axial velocity and all axial gradients of the other variables were zero at the symmetry plane so that $U=0$, $\mathrm{d}V/\mathrm{d}z=\mathrm{d}P/\mathrm{d}z=\mathrm{d}k/\mathrm{d}z=\mathrm{d}\varepsilon/\mathrm{d}z=0$. A constant pressure equal to the

atmospheric value (1 bar, 10^5 Pa) was applied at the pressure boundaries so that $P = P_{atm} = 10^5$ Pa and the gradients of all variables normal to the pressure boundary were set equal to zero, i.e. $dU/dz = dV/dz = dk/dz = d\varepsilon/dz = 0$ at the pressure boundary parallel to the stagnation plane while $dU/dr = dV/dr = dk/dr = d\varepsilon/dr = 0$ at the pressure boundary parallel to the axis.

The mean radial velocity was zero at the axis of symmetry so that $V = 0$, while the radial gradients of all other variables were zero, i.e. $dP/dr = dU/dr = dk/dr = d\varepsilon/dr = 0$. Zero azimuthal flow boundaries were also indicated in Figure 1 so that $d/d\theta = 0$.

3. NUMERICAL PROCEDURE AND UNCERTAINTIES

The computations were carried out using a computer (INTEL 800 MHz, 256 MB) to 64-bit precision in conjunction with available software (STAR-CD, Absoft FORTRAN). The convergence times for calculations with two operating systems (LINUX, WINDOWS 2000) were compared and those with the LINUX system were typically between 15 and 20% faster, requiring around 48h of CPU time per run depending on the mesh density and dimensions, and it was used for the subsequent calculations in this paper. The equations were discretized and solved using the finite volume method in conjunction with the SIMPLE algorithm as explained by many authors including Versteeg and Malalasekera [51], Patankar [52] and Ferziger and Peric [53]. The conjugate gradient method was the iterative diagonalization procedure of Kershaw [54], and it was implemented in FORTRAN.

The QUICK differencing scheme was used together with a distributed grid that was refined in regions of high gradients to ensure that Peclet numbers were below 2.7 and this allowed smooth convergence of the third-order numerics as well as reducing the effects of numerical diffusion. Convergence was assumed after 5000 iterations at which the fractional change in the values of all quantities averaged over the entire solution domain reduced by at least four orders of magnitude and further iterations had no effect on the final solution. Although an expression for the effective numerical diffusivity for two-dimensional problems using first-order numerics was given by (de Vahl Davis and Mallinson) [55], no such expression exists for higher order schemes where the effects of numerical diffusion are expected to be smaller.

3.1. Grid tests

The pressure boundaries were initially set at a radial distance of 5.0 D from the axis and 2.5 D from the stagnation plane, i.e. $L_{out} = 5.0\ D$ and $L_{pres} = 2.5\ D$ as in Figure 1(a), and the inlet boundary was located 2.0 D upstream of the nozzle exit, $L_{in} = 2.0\ D$. The consequences of the position of the boundaries, particularly the inlet boundary, were examined with results summarized in the following subsection. A bulk velocity of 3.3 m/s, corresponding to a Reynolds number based on exit diameter of 5500, was chosen to allow equivalent grid tests in laminar and turbulent flows. The nozzle separation of 1.0 D implied that the grid nodes were distributed over a rectangular solution domain of axial dimension 2.5 D and radial dimension 5.0 D. Four successively refined uniform grids: 30×60, 60×120, 125×250 and 250×500 were examined together with one redistributed grid with 6785 nodes to provide the highest resolution in regions of high velocity gradient, as discussed further below. The following paragraphs present the results of the grid tests in laminar and turbulent flows. Profiles at the exit plane were from the axis to the wall, $r = 0$ to R where $R = 0.5\ D$, those at the axis from

the stagnation plane to the inlet boundary, $z = 0.0$ to 2.5 D, and those at the stagnation plane from the axis to the pressure boundary, $r = 0.0$ to 10.0 R.

For laminar flow, the profiles of all the variables varied by less than 3% close to the axis, even with the 30×60 mesh, and the same agreement was achieved at mesh densities of 125×250 or greater in the region of high velocity gradient close to the wall. The need for higher mesh densities near the wall defined a maximum cell dimension of 0.5 mm at the wall and 2.1 mm at the axis and guided the construction of the distributed grid using a geometric series with an initial cell width of 0.2 mm, and successive increases of 7% to a maximum of 1.1 mm at the axis. The distributed grid had 6785 nodes, 22% less than the uniform 125×250 mesh, and often converged with at least a four-fold reduction in computational time. The effects of the grid on the flow on the axis were less than 3%, again with mesh densities of 125×250 and greater and with the distributed grid. The profiles of pressure on the stagnation plane were also affected by less than 3% and the radial velocities agreed to within 1% even at the lowest mesh density, 30×60, within 1.5 R of the axis and in the region of interest where experimental observations in Reference [25] showed that the flame was stabilized and extinction eventually occurred. Higher mesh density were required at larger radii.

For turbulent flow, profiles of pressure and two components of mean velocity at the nozzle exit were within 5% of each other with all grids. Profiles of the rms of the velocity fluctuations and the integral length scale were within 3%. Calculated pressures along the axis varied by less than 10% and velocities by less than 5%. Calculated profiles of pressure and velocity at the stagnation plane were affected by less than 3% and rms velocities and length scales by less than 15%.

In summary, the distributed grid produced profiles and distributions of all calculated quantities that agreed with the two finest uniform meshes and convergence was achieved in one quarter of the time so that the distributed grid was used throughout the rest of the calculations in this paper.

3.2. Assessment of boundary condition assumptions

The axial and radial distances from the stagnation plane and axis of symmetry of the two pressure boundaries were defined in Figure 1(a) as $L_{\text{pres}} + H/2$ and L_{out} and their minimum values, to ensure that they did not affect the flow solutions, were a function of mesh density. Coarser meshes generally required pressure boundaries further from the stagnation region and repeated trials showed that the conditions $L_{\text{out}} = 5.0\ D$ and $L_{\text{pres}} = 2.0\ D$ were sufficient for the range of grids tested and were adopted for all the calculations in this paper. The inlet boundary was located 2.0 D upstream of the nozzle exit, i.e. $L_{\text{in}} = 2.0\ D$ in Figure 1(a), for the grid dependence studies above and preliminary calculations of the exit flow showed that there was no change in calculated profiles of pressure at the exit for values of L_{in} greater than 1.00 D, but smaller values increased the pressure by a factor of up to two at $L_{\text{in}} = 0.00\ D$ at the axis while the pressure at the edge of the pipe wall at $r/R = 1.0$ was reduced. A bulk velocity of 0.645 m/s was chosen for these calculations, corresponding to a Reynolds number based on diameter of 1000, as a laminar flow of a pipe separation of 0.2 D because they produced the largest effects of L_{in} on the flow.

Distributions of pressure and velocity along the axis confirmed that any choice of $L_{\text{in}} < 1.00\ D$ resulted in an increase of the pressures and velocities along the stagnation stream-

line, by a factor of up to 2, while pressures in the stagnation plane also increased within 0.5 R of the axis. Profiles of radial velocity on the stagnation plane increased to a peak of up to $3.8U_b$ at $r/R = 1.0$ with $L_{in} = 0.00$ D and the peak was at $r/R = 1.2$ with larger values of L_{in} where the amplitude was 40% smaller.

As a consequence of the above, $L_{in} = 2.0$ D was used for the remaining calculations in this paper.

4. RESULTS

The results are presented in three subsections dealing with inviscid, laminar and turbulent flows respectively and each describing the flow at the exit, along the axis and at the stagnation plane. The brief subsection on inviscid flows showed the extent to which an inviscid inlet boundary, applied 2 D upstream of the exit, was able to reproduce the non-uniformities downstream that were evident in the viscous flows where viscosity was a perturbation. The Reynolds number is important in laminar flows, except in regions where similar solutions may exist such as far downstream in the radial jet of the opposed flow and, since it is unlikely that a similarity parameter can characterize the impingement region where non-uniformities exist, calculations are reported for four Reynolds numbers ranging from 170 to 2500. Thus, the effects of bulk velocity, nozzle separation and pipe or nozzle boundary conditions are discussed respectively for laminar and turbulent flows and are compared qualitatively with past measurements and quantitatively with those at the exit and stagnation planes from Korusoy and Whitelaw [25]. The results of the Jones and Launder, Chen and Kim, and RNG turbulence models, discussed above, are also compared with measurements to assess accuracy and possible benefits of the latter two models at the stagnation plane. The emphasis is, however on the calculations of local strain rate and their implications. All static pressures are normalized by the bulk dynamic pressure, $0.5\rho U_b^2$.

4.1. Inviscid flow

Figures 2–4 show inviscid-flow normalized pressures and velocity in the exit plane, along the axis and on the stagnation plane for a bulk velocity of 0.645 m/s and as a function of nozzle separation, and Figure 5 shows the strain rates on the stagnation plane.

The exit-plane pressures of Figure 2(a) increased to $36\rho U_b^2$ close to the axis as the separation reduced to 0.2 D and reached that of the surroundings at $r = 1.0$ R. The axial velocities of Figure 2(b) show a constant region near the axis with a peak at 1.0 R where there was a finite slip-velocity at the wall and no boundary layer. The axial velocity at the peak increased from 1.0 to $3.0U_b$ as the separation was reduced from 2.0 to 0.2 D and the minimum at the axis fell from 1.0 to 0.3 U_b. The profiles of radial velocity, Figure 2(c), show increasing flow from the axis with smaller separations, as expected from continuity, and the peak in radial velocity moved towards the wall until it reached 0.92 R at the separation of 0.2 D where its amplitude was 0.98 U_b. Thus, the solution of the inviscid flow equations exhibited non-uniformities at the exit with separations of 1.0 D or less, in common with experiments.

The distribution of normalized pressure *along the axis*, Figure 3(a), has a constant region upstream and a peak at the stagnation point. The pressure in the constant region increased from near zero to 8 ρU_b^2 as the nozzle separation was reduced from 2.0 to 0.2 D while the

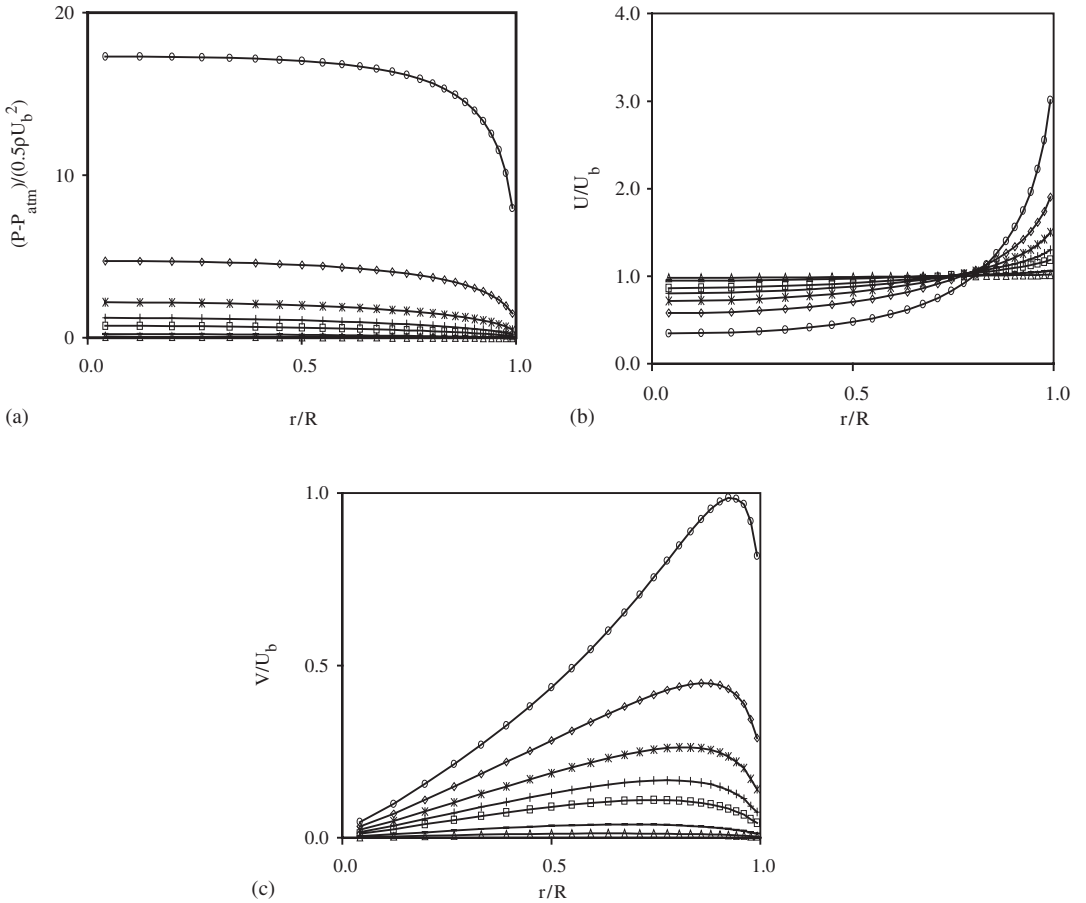

Figure 2. Profiles of normalized pressure and velocity at the exit as a function of H/D: (a) pressure; (b) axial velocity; and (c) radial velocity. Inviscid flow, $U_b = 0.645$ m/s ∘ (0.20); ◇ (0.40); * (0.6) + (0.80); □ (1.0); − (1.5) △ (2.0).

stagnation pressure increased from 0.5 to 8.5 ρU_b^2. Thus, the distribution of axial velocity was also constant upstream of the exit plane, at U_b, and reduced to zero at the stagnation point. It is evident from Figure 3(b), that the axial velocity gradient and hence the strain rate at the stagnation point increased non-linearly from 50 to 97/s with separation from 2.0 to 0.2 D at the bulk velocity of 0.645 m/s. The commonly used bulk strain rate formula, $2U_b/H$, produced values that increased from 52 to 516/s, with the same range of separation. The bulk strain rate increasingly overestimated the local strain rate at the stagnation point, to a factor of up to 3.8 as the separation of $0.2D$, because the assumption of uniform conditions upstream was increasingly invalid as the separation was reduced.

Profiles of pressure at the *stagnation plane*, Figure 4(a), have a peak at the stagnation point equal to the stagnation pressure and became broader and the pressure increased as the

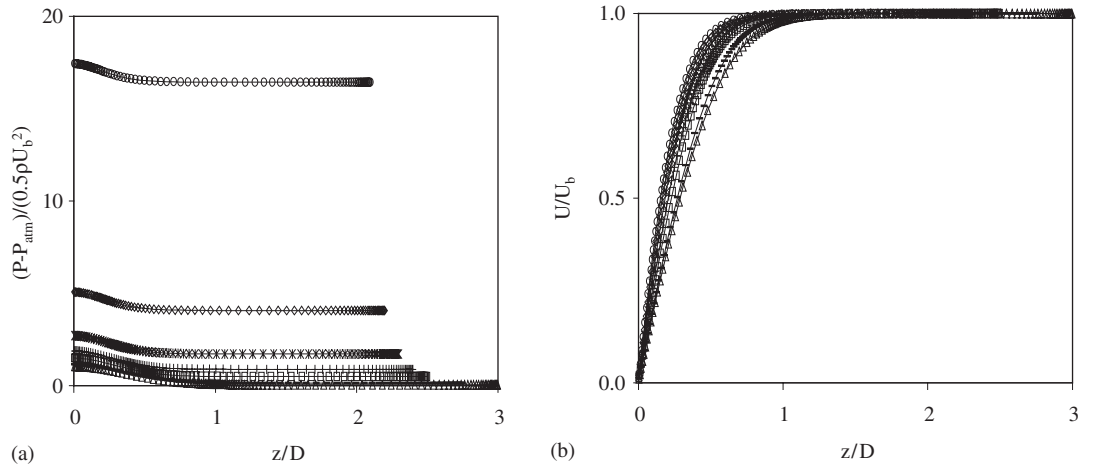

Figure 3. Distributions of normalized pressure and velocity along the axis as a function of H/D: (a) pressure; and (b) axial velocity. $U_b = 0.645$ m/s, Inviscid flow ∘ (0.20); ◇ (0.40); * (0.6) + (0.80); □ (1.0); – (1.5) △ (2.0).

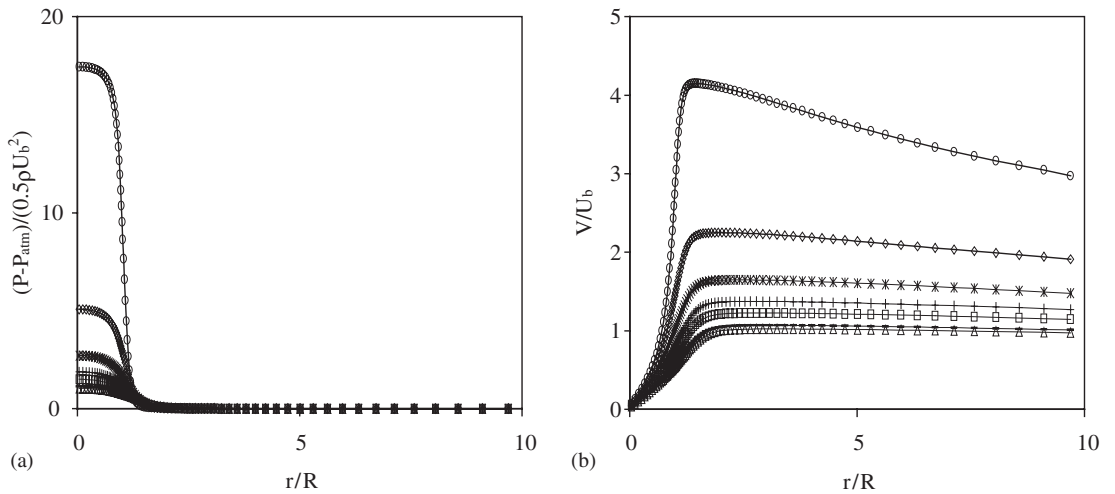

Figure 4. Profiles of normalized pressure and velocity on the stagnation plane as a function of H/D: (a) pressure; and (b) axial velocity. $U_b = 0.645$ m/s, Inviscid flow ∘ (0.20); ◇ (0.40); * (0.6) + (0.80); □ (1.0); – (1.5) △ (2.0).

separation was reduced from 2.0 to 0.2 D. The pressure decreased with radial distance from the axis until it was equal to the surroundings at a radius that increased from 1.3 to 2.0 R with the same reduction in separation. Thus, the corresponding profiles of radial velocity, Figure 4(b), increased from zero at the axis to a peak at radii that increased from 1.3 to

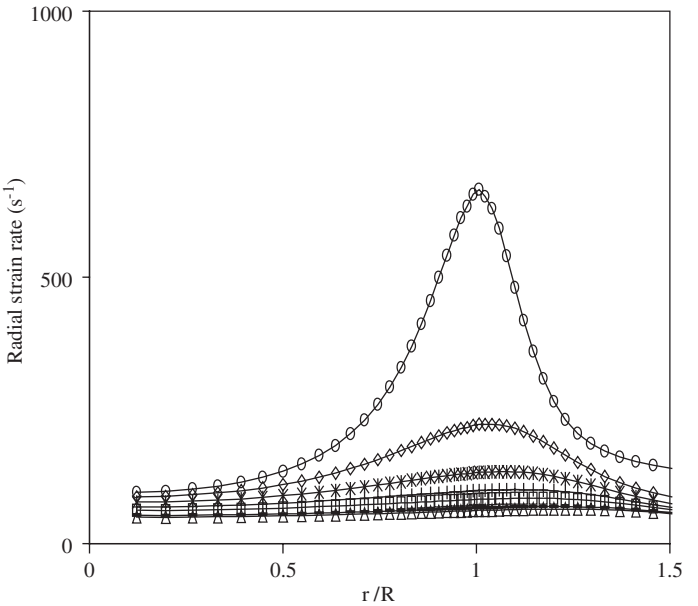

Figure 5. Profiles of radial strain rate on the stagnation plane as a function of H/D. $U_b = 0.645$ m/s, Inviscid flow ∘ (0.20); ◇ (0.40); * (0.6) + (0.80); □ (1.0); − (1.5) △ (2.0).

2.0 R as the separation was reduced from 0.2 to 2.0 D and this also led to an increase in peak radial velocity, from 1.0 to 4.1 U_b, as expected from the increase in stagnation pressure. The decay in radial velocity after the peak, was due to continuity as the flow spread into the surroundings.

Continuity required the magnitude of the axial and radial components of strain rate to be equal at the stagnation plane and profiles of radial strain rate are presented in Figure 5. The minimum strain rate occurred at the axis and reached a maximum at a radial distance that decreased to 1.0 R as the separation was reduced to 0.2 D. The position of the peak in strain rate was increasingly difficult to determine with increasing separation because of the reduction in its amplitude. The results at smaller separations suggest that the maximum in radial velocity was approximately twice as far from the axis as the maximum in radial strain rate. The minimum strain rate at the axis increased from 50 to 97/s as the nozzle separation was reduced from 2.0 to 0.2 D while the maximum values increased from 65 to 665/s, suggesting that there was still a slight peak in strain rate even at the separation of 2.0 D. The strain rates at the peak and axis as a function of separation are summarized in Table IV at the bulk velocity of 0.645 m/s and values at other bulk velocities may be obtained by linear extrapolation. Again, the trends are similar to those of the experiments of Korusoy and Whitelaw [25].

4.2. Laminar flow

Figures 6–9 present results for laminar flow with the first two showing the effects of Reynolds number and nozzle separation on pressure and velocities on the exit and stagnation planes and

Table IV. Strain rate on the axis of the symmetry plane and the peak value as a function of H/D with inviscid flow, $U_b = 0.645$/s.

H/D	S_{axis} (s^{-1})	S_{peak} (s^{-1})
2.0	50	65
1.5	53	69
1.0	62	85
0.8	69	101
0.6	78	135
0.4	88	224
0.2	97	665

the second two concerned with strain rate profiles on the stagnation plane and, in the case of Figure 9, with the differences caused by opposed nozzles and pipes.

The pressure across the *exit planes* of the opposed nozzles, Figure 6(a), was equal to that of the surroundings at all bulk velocities when the separation was 2.0 D, and this implies that a stagnation plane 1.0 D downstream had no effect on the flow at the exit. The normalized pressure increased with reduction in nozzle separation and there was also a small increase with bulk velocity. Pressures at the axis ranged from 7 to 8 ρU_b^2 as the bulk velocity increased from 0.1 to 1.5 m/s, corresponding to Reynolds numbers from 170 to 2500. Comparison with the inviscid flow calculations revealed values up to 5% greater with viscous laminar flow and that the former reproduced the trend that pressure increased with reduction in separation.

Effects of pipe or nozzle upstream boundary conditions are evident in Figure 7(a), at the Reynolds number of 1000 and over a range of separations from 0.2 to 2.0 D, where the pressure at the exit of the nozzle was generally smaller than that of the pipe, particularly towards the wall where differences in boundary layer thickness are expected. They were small for nozzle or pipe separations greater than 1.0 D but increased with reduction in separation until the static pressures at the axis were 7.5 ρU_b^2 and 8.0 ρU_b^2 for a nozzle and pipe at the smallest separation of 0.2 D. These results suggest that the stagnation plane had an increasing influence on the flow at the exit as the separation was reduced below 1.0 D.

It is apparent from profiles of axial velocity in Figure 6(b) that the boundary layer thickness decreased from 0.67 to 0.17 R at the separation of 2.0 D, as the Reynolds number increased from 270 to 2500, and that the position of the peak in the profile of axial velocity at the separation of 0.2 D was away from the wall by a distance that decreased from 0.04 to 0.01 R. Viscous friction reduced the peak in axial velocity by up to 30%. The axial velocity on the axis of the nozzle exit decreased from 1.19 to 0.38 U_b with reduction in separation from 2.0 to 0.2 D, Figure 7(b), and there was a minimum at the axis with separations less than 1.0 D. In contrast, the velocity on the axis of the pipe was about twice that of the nozzle and had a broad peak at the axis at all separations. All velocity profiles exhibited a peak of increasing amplitude close to the wall as the nozzle separation was reduced below 1.0 D and the amplitude of the peak was about 20% greater for the nozzles as a consequence of the minimum at the axis and continuity.

There was almost no radial flow at the nozzle separation of 2.0 D, Figure 6(c), while the favourable radial pressure gradient led to strong radial flow from the axis with smaller separations and flow angles were up to 45° at 0.2 D. The increase in boundary layer thick-

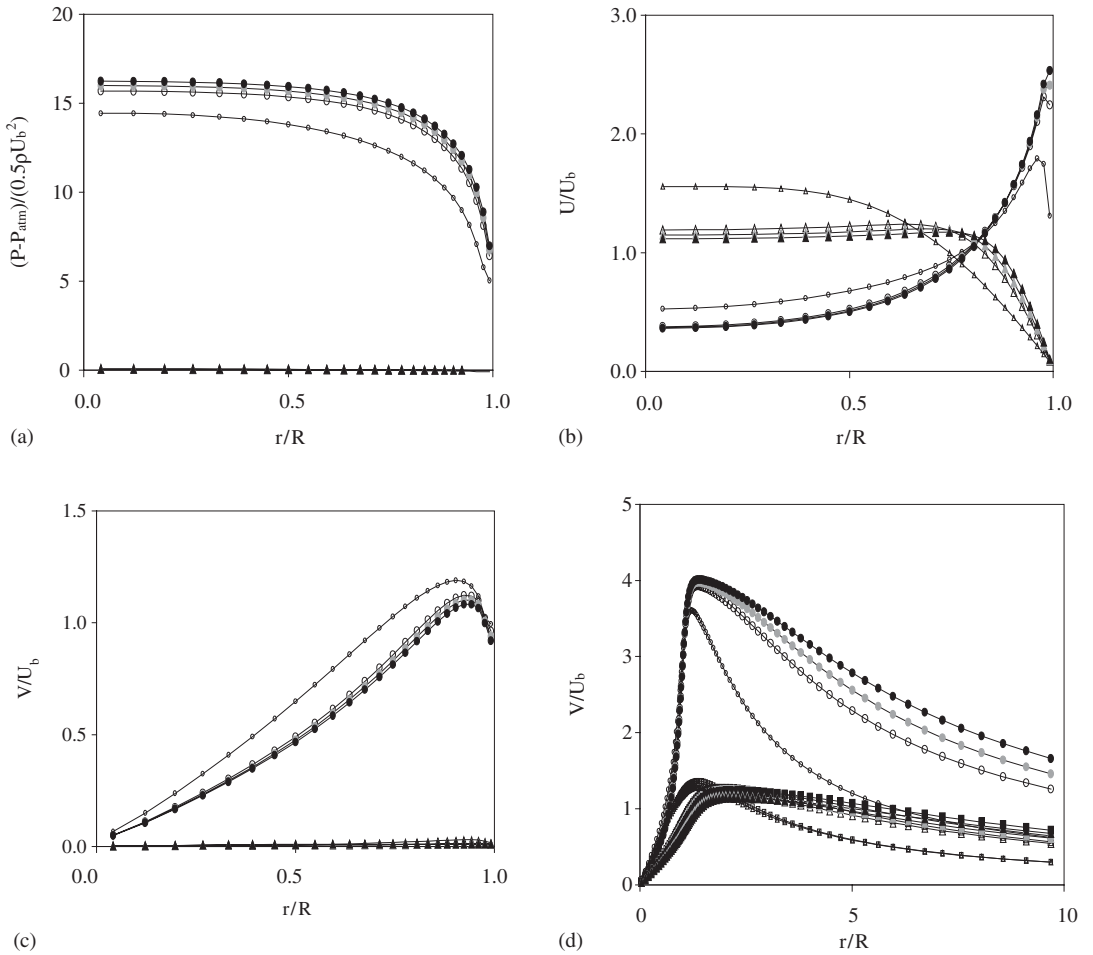

Figure 6. Profiles of pressure and velocity on the exit and stagnation planes as a function of U_b for two nozzle separations: (a) pressure at the exit; (b) axial velocity at the exit; (c) radial velocity at the exit; and (d) radial velocity at the stagnation plane. $H/D = 0.2$; ∘ (0.100 m/s); ◯ (0.645 m/s); • (1.000 m/s); ● (1.500 m/s); $H/D = 2.0$; △ (0.100 m/s); ■ (0.645 m/s); ▲ (1.000 m/s); ∗ (1.500 m/s). Velocities correspond to laminar flow with Reynolds numbers of 170, 1000, 1700, 2500.

ness at low Reynolds numbers meant that the flow was increasingly distributed towards the axis and continuity required a larger normalized radial flow to achieve the minimum in the axial velocity in Figure 6(b). This explained the increase in normalized radial velocity with reduction in Reynolds number in Figure 6(c). It is evident that the radial velocities in the inviscid flow were only 3% greater than that of laminar nozzles at the separation of 0.2 D. A reduction in nozzle or pipe separation led to increasing radial flow, Figure 7(c), due to the increase in radial pressure gradient in Figure 7(a) and as required by continuity to allow the minimum in axial flow in Figure 7(b). The radial velocity at the exit of the pipe was greater

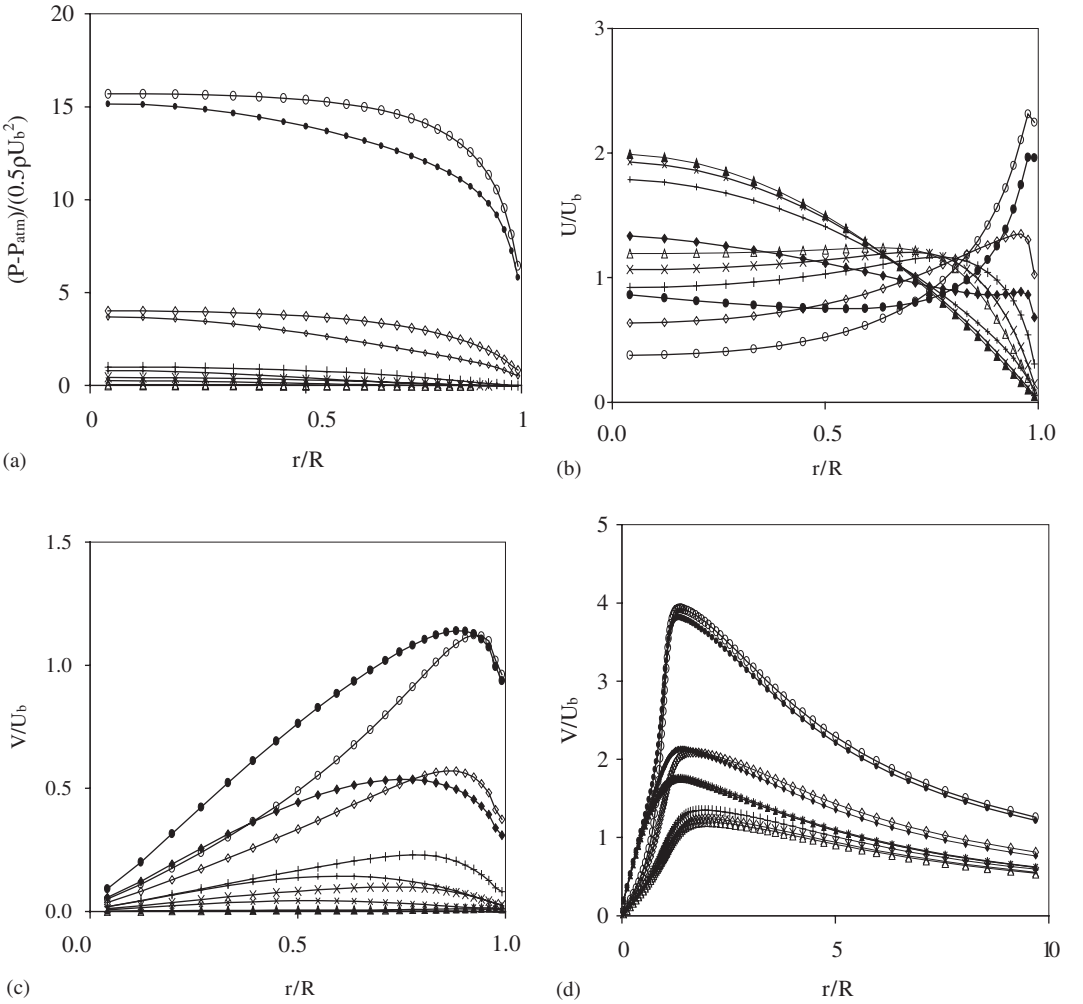

Figure 7. Profiles of pressure and velocity on the exit and stagnation planes as a function of H/D: (a) pressure at the exit; (b) axial velocity at the exit; (c) radial velocity at the exit; and (d) radial velocity at the stagnation plane. $U_b = 0.645\,\mathrm{m/s}$, $\mathrm{Re} = 1000$, Laminar flow. Nozzle: ○ (0.20); ◇ (0.40); + (0.80); × (1.14) △ (2.00). Pipe: ● (0.20); ◆ (0.40); + (0.80); × (1.14) ▲ (2.00).

than that of the nozzle, by a factor of up to two towards the wall as a consequence of the larger radial pressure gradient.

Distributions of normalized pressure *along the axis* of opposed nozzles were qualitatively similar at all bulk velocities and separations with a peak at the stagnation point followed by a decay to a minimum upstream of the exit followed by an increase towards the inlet boundary. The pressure at all points along the axis scaled with bulk velocity in the same way as the pressure at the axis of the exit plane described above. The stagnation pressure increased from 7.5 to 8.0 ρU_b^2, while corresponding pressures at the minimum increased from 6.5 to 7.5 ρU_b^2

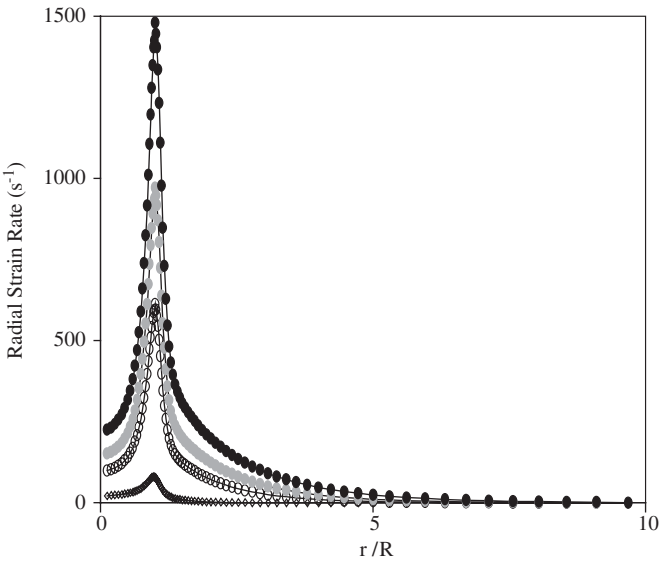

Figure 8. Profiles of radial strain rate on the stagnation plane as a function of U_b. $H/D = 0.2$: ○ (0.100 m/s); ◯ (0.645 m/s); • (1.000 m/s); ● (1.500 m/s). Velocities correspond to laminar flow with Reynolds numbers of 170, 1000, 1700, 2500.

and those at inlet boundary increased from 7.0 to 7.5 ρU_b^2, as the bulk velocity increased from 0.1 to 1.5 m/s, corresponding to Reynolds numbers from 170 to 2500, at the pipe separation of 0.2 D. The position of the minimum was unaffected by bulk velocity but moved further from the stagnation plane, from 0.5 to 1.0 D, as the separation increased from 0.2 to 2.0 D and the same increase in separation reduced all pressures along the distribution to less than 1.5 ρU_b^2. The pressures along the axis of opposed pipes were simpler than those of nozzles, and had a similar peak at the stagnation point followed by decay to a constant value upstream of the exit, and the shape of the distributions was similar to that of the inviscid flows except that the inviscid stagnation pressure was 8% higher. The pressures along the axis of opposed pipes were generally greater, by up to 25%, than with nozzles so that the stagnation pressure increased from 2 to 8 ρU_b^2 while the value upstream increased from 0 to 6 ρU_b^2 as the pipe separation was decreased from 2.0 to 0.2 D at the bulk velocity of 0.645 m/s. The distributions of pressure along the axis of opposed pipes scaled with bulk velocity in the same way as the nozzle flows above.

The axial strain rate at the *stagnation point* increased from 23 to 246/s as the bulk velocity increased from 0.1 to 1.5 m/s with the nozzle separation of 0.2 D. The strain rate reduced with increasing nozzle or pipe separation from 0.2 to 2.0 D and values ranged from 99 to 60/s for nozzles at the bulk velocity of 0.645 m/s, and a much smaller reduction from 269 to 254/s for opposed pipes. The inviscid flow calculations produced axial strain rates that were generally 30% greater than the laminar flow calculations.

These results show that the effect of separation on strain rates was much greater for opposed nozzles than pipes and highlights the importance of upstream conditions and the inadequacy of the bulk strain rate formula, $2U_b/H$, which produced equal strain rates for pipes and nozzles

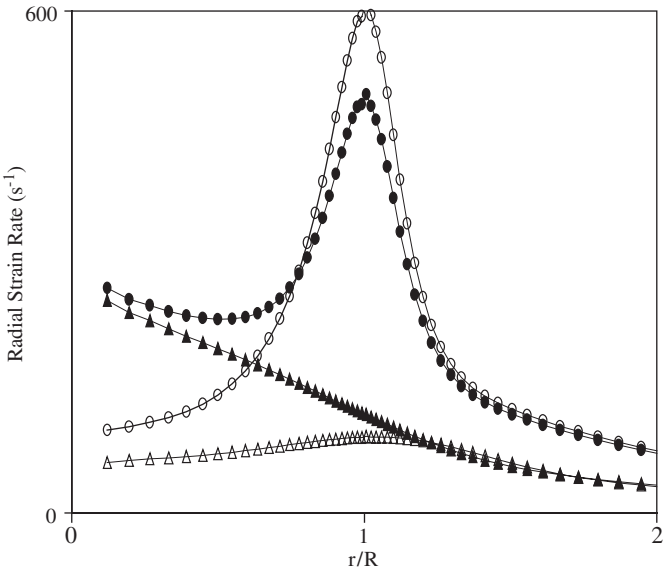

Figure 9. Profiles of radial strain rate on the stagnation plane for a nozzle and a pipe at two separations. $U_b = 0.645$ m/s, Re = 1000, laminar flow. Nozzle: ○ (0.20); △ (2.00). Pipe: • (0.20); ▲ (2.00).

ranging from 52 to 516/s, and increasingly overestimated local values by a factor of up to 5 for nozzles and 2 for pipes towards the smallest separation of 0.2 D.

Profiles of pressure on the stagnation plane had a peak equal to the stagnation pressure and decreased with distance from the axis until it was equal to that of the surroundings at radii greater than 2 R and the shape was qualitatively similar to those of the inviscid flows with which a reduction in separation broadened the peak. The decay in pressure was faster with opposed pipes than nozzles due to the greater stagnation pressure. Profiles of radial velocity at the stagnation plane, Figure 6(d), increased from zero at the axis to a peak, beyond which entrainment and continuity led to a reduction. The peak moved, from 1.3 to 1.4 R as the Reynolds number increased from 170 to 2500, at the nozzle separation of 0.2 D. It is also evident in Figure 7(d) that an increase in nozzle separation from 0.2 to 2.0 D moved the peak from 1.4 to 1.9 R at the Reynolds number of 1000 and this was because the flow was spread over a larger area of impingement at the stagnation plane.

The stagnation plane formed the axis of a radial jet and similar solutions for the boundary layer equations in the far field suggest that the radial velocity far downstream along the stagnation pane decays according to the inverse square of the radial distance from a virtual origin. This inverse square law was obeyed to within 1% at distances greater than 7 R from the axis. The position of the virtual origin varied from -3.6 to -5.2 R. Continuity required axial and radial strain rates to be of equal magnitude and the radial strain rate at the stagnation plane of opposed nozzles with separation 0.2 D increased to a peak at 1.0 R as shown in Figure 8. The radial strain rate increased with bulk velocity and the value at the peak increased from 65 to 1476/s with bulk velocities from 0.1 to 1.5 m/s. The peak is shown on a magnified scale in Figure 9 at the two extremes of separation. It is evident that the amplitude of the

Table V. Strain rates at the axis of the symmetry plane and the peak value as a function of H/D for laminar and turbulent pipe and nozzle flow.

	Laminar, $U_b = 0.645$ m/s, Re = 1000				Turbulent, $U_b = 3.3$ m/s, Re = 5500			
	Nozzles		Pipes		Nozzles		Pipes	
H/D	S_{axis} (s^{-1})	S_{peak} (s^{-1})	S_{axis} (s^{-1})	S_{peak} (s^{-1})	S_{axis} (s^{-1})	S_{peak} (s^{-1})	S_{axis} (s^{-1})	S_{peak} (s^{-1})
2.0	60	91	254	—	180	230	194	233
1.0	63	95	254	—	241	319	249	302
0.8	69	107	256	—	293	409	313	399
0.4	89	207	262	—	455	937	511	935
0.2	99	612	269	501	521	2642	596	2660

peak in radial strain rate was greatly diminished, from 612 to 91/s, as the nozzle separation increased from 0.2 to 2.0 D.

The effects of pipe and nozzle boundary conditions are also shown in Figure 9 where the profile of radial strain rate for the opposed pipes with separation 0.2 D has a broad peak at the axis of amplitude 269/s, rather than the minimum observed with nozzles. The amplitude of the peak at the axis of opposed pipes was smaller than that at 1.0 R, where the strain rate was 501/s. The strain rate at the axis of the opposed nozzles was smaller than that of the pipes while the strain rate at 1.0 R was greater for the nozzles. Strain rates calculated in laminar flows were generally some 11% less than those in inviscid flows suggesting that a good estimate of local strain rates could be achieved without the complication of viscosity. The strain rates at the axis and peak are summarized as a function of separation for nozzles and pipes in Table V at the Reynolds number of 1000. Values at higher Reynolds numbers may be estimated by linear extrapolation with the caveat that it leads to underestimation by up to 34% at the Reynolds number of 5500.

The peak in strain rate at 1.0 R at small pipe or nozzle separations suggests that local quenching should occur in laminar opposed flames initially at 1.0 R from the axis with growth of the quenched region towards the axis as the bulk velocity was increased to complete extinction. The main difference between pipes and nozzles was the additional peak in strain rate at the axis of pipes and the smaller amplitude of the peak at 1.0 R. This suggests that quenching at 1.0 R would occur earlier in nozzles than pipes, with quenching at the axis occurring earlier in pipes. It remains to be seen whether the latter would cause complete extinction. Thus, the bulk velocity at which local quenching occurs for laminar flames in opposed nozzles with H/D of 0.2 is smaller than that of pipes, although the bulk velocity at complete extinction may be greater.

4.3. *Turbulent flow*

The calculated results for turbulent flows are presented in Figures 10–16 and involve comparisons with measurements and the three turbulence models. It is of note that the turbulence models did not affect values of pressure or velocity by more than 3% so that related comments are brief.

The pressure at the *exit plane* of opposed flows, Figure 10, was constant at 2.2 ρU_b^2 to within 3% for bulk velocities from 0.85 to 3.40 m/s at the nozzle separation of 0.4 D, chosen to correspond to the experiments of Korusoy and Whitelaw [25]. The calculated

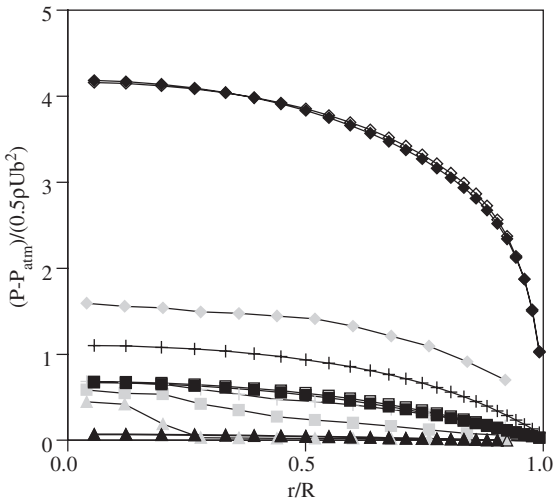

Figure 10. Profiles of normalized mean pressure at the exit as a function of H/D. $U_b = 3.3$ m/s, Re = 5500, turbulent flow. Nozzles: ◇ (0.4); + (0.8) □ (1.0); △ (2.0). Pipes: ◆ (0.4); + (0.8) ■ (1.0); ▲ (2.0). Measurements: ◆ (0.4); + (0.8) ■ (1.0); ▲ (2.0).

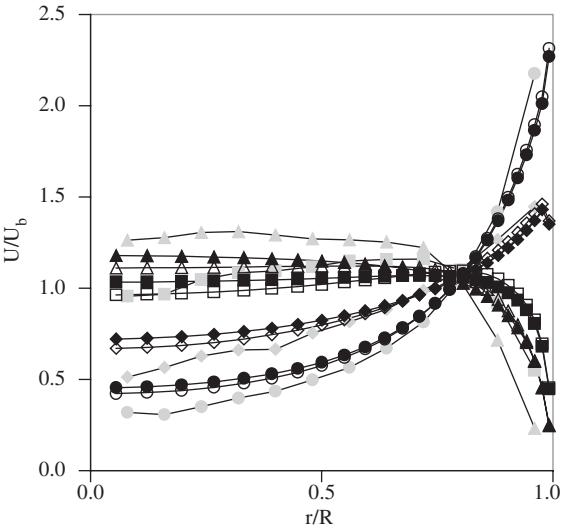

Figure 11. Profiles of normalized mean axial velocity at the exit as a function of H/D. $U_b = 3.3$ m/s, Re = 5500, turbulent flow. Nozzles: ○ (0.2) ◇ (0.4); □ (1.0); △ (2.0). Pipes: • (0.2) ◆ (0.4); ■ (1.0); ▲ (2.0). Measurements: • (0.2) ◆ (0.4); ■ (1.0); ▲ (2.0).

and measured values display similar trends and confirm the scalability of static pressure with U_b^2 but the calculated value at the axis increased from near zero with a separation of 2 D to 8 ρU_b^2 with 0.2 D, while a much smaller increase, from zero to 0.9 ρU_b^2,

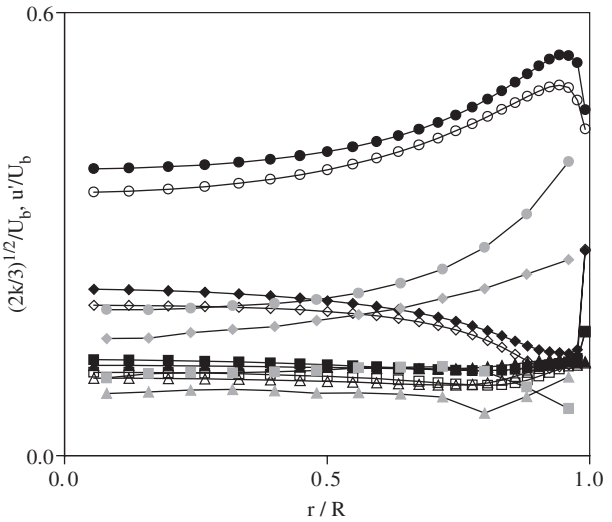

Figure 12. Profiles of normalized axial velocity fluctuations at the exit as a function of H/D. $U_b = 3.3$ m/s, Re = 5500, turbulent flow. Calculations with Jones and Launder (1972) model: Nozzles: ○ (0.2) ◇ (0.4); □ (1.0); △ (2.0). Pipes: ● 0.2 ◆ (0.4); ■ (1.0); ▲ (2.0). Measurements: ● (0.2) ◆ (0.4); ■ (1.0); ▲ (2.0).

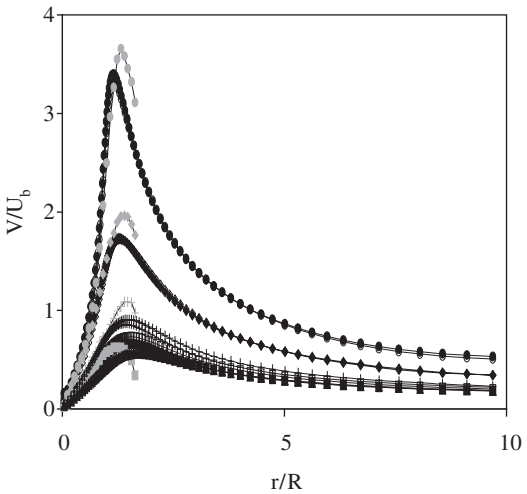

Figure 13. Profiles of normalized mean radial velocity on the stagnation plane as a function of H/D. $U_b = 3.3$ m/s, Re = 5500, turbulent flow. Nozzles: ○ (0.2); ◇ (0.4); + (0.8); □ (1.0); △ (2.0). Pipes: ● (0.2); ◆ (0.4); + (0.8); ■ (1.0); ▲ (2.0). Measurements: ● (0.2); ◆ (0.4); + (0.8); ■ (1.0).

was observed as the nozzle separation was reduced to 0.4 D. Corresponding values of pressure at the exit of opposed pipes were within 3% of the nozzles. The ability of the calculations to reproduce correct trends with bulk velocity and nozzle separation

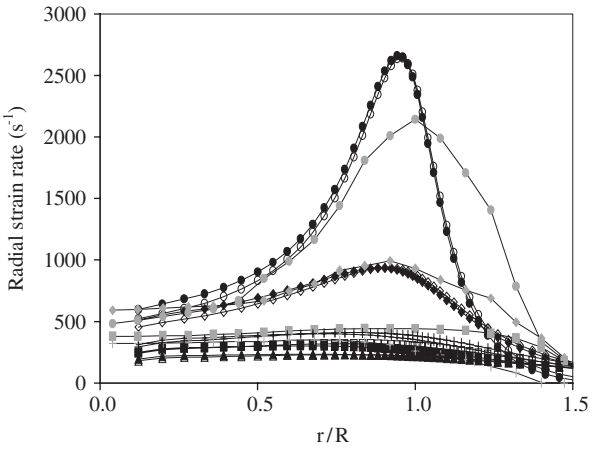

Figure 14. Profiles of normalized mean radial strain rate on the stagnation plane as a function of H/D. $U_b = 3.3$ m/s, Re = 5500, turbulent flow. Nozzles: ○ (0.2); ◇ (0.4); + (0.8); □ (1.0); △ (2.0). Pipes: • (0.2); ◆ (0.4); + (0.8); ■ (1.0); ▲ (2.0). Measurements: • (0.2); ◆ (0.4); + (0.8); ■ (1.0).

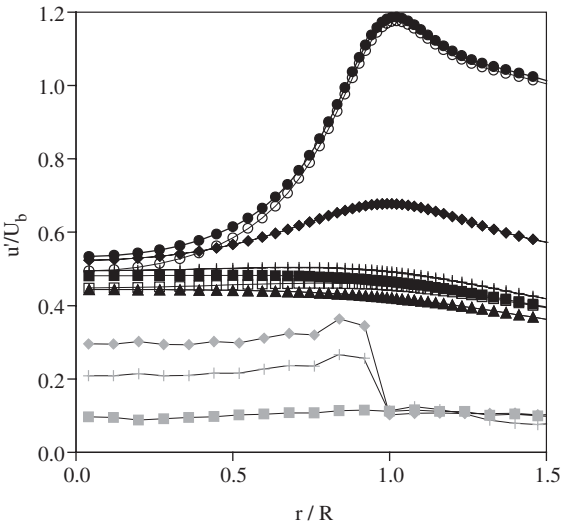

Figure 15. Profiles of normalized rms velocity fluctuations on the stagnation plane as a function of H/D. $U_b = 3.3$ m/s, Re = 5500, Jones and Launder model. Nozzles: ○ (0.2); ◇ (0.4); + (0.8); □ (1.0); △ (2.0). Pipes: • (0.2); ◆ (0.4); + (0.8); ■ (1.0); ▲ (2.0). Measurements: ◆ (0.4); + (0.8); ■ (1.0).

is encouraging, although the measured pressure was overestimated by factors of up to 2.4.

The normalized axial velocity decreased at the axis from 0.76 to 0.72, as U_b ranged from 0.85 to 3.40 m/s with the nozzle separation of 0.4 D and the same increase in bulk velocity moved the peak closer to the wall, from 0.96 R to 0.98 R. It is evident in Figure 11 that

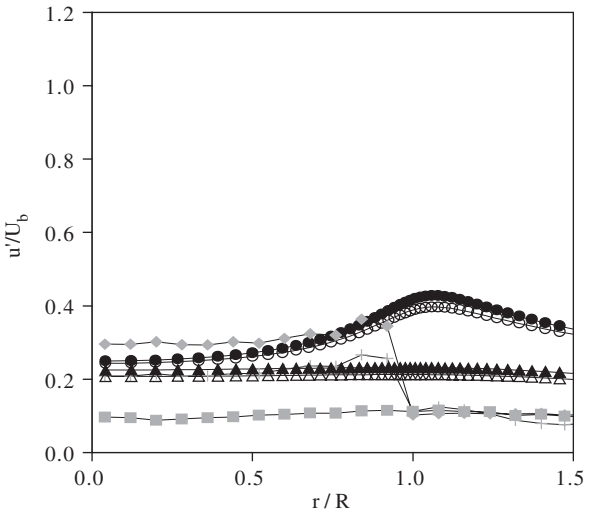

Figure 16. Profiles of normalized rms velocity fluctuations on the stagnation plane as a function of H/D. $U_b = 3.3$ m/s, Re = 5500. RNG model: ○ (0.2); △ (2.0). Chen and Kim model: • (0.2); ▲ (2.0). Measurements: ♦ (0.4); + (0.8); ■ (1.0).

a reduction in nozzle separation from 2.0 to 0.2 D led to a reduction in axial velocity at the axis from 1.0 to 0.4 U_b, and that there was a maximum of increasing amplitude near the wall with nozzle separations less than 1.0 D. The amplitude of the peak increased to 2.1 U_b as the separation was reduced to 0.2 D. The measured axial velocity close to the axis was underestimated by up to 17% at separations greater than 1.0 D, Figure 11, and overestimated by up to 11% towards the smallest separation of 0.2 D. Continuity meant that the situation was reversed near the wall where measured axial velocities were overestimated at large separations and underestimated at small ones, but the discrepancy at separations less than 1.0 D was less than 5%. The profiles of axial velocity at the exit of nozzles and pipes both show a minimum at the axis and a peak near the wall and the shapes are qualitatively similar. This is in contrast to the laminar flows where the pipe had a broad peak at the axis, and the largest quantitative differences were on the axis and at the largest separation of 2.0 D.

The radial velocity increased from zero at the axis to a peak at 0.9 R after which there was a sharp reduction to zero at the nozzle wall and the amplitude of the peak decreased from 0.54 to 0.49 U_b, as the bulk velocity increased from 0.85 to 3.40 m/s. The amplitude of the peak increased from zero to U_b with nozzle separation reduced to 0.2 D and that the value for pipes was within 3% of those of nozzles. Profiles of radial velocity measured with a hot wire by Korusoy and Whitelaw [25], agreed with the calculations to within 5% at radii greater than 0.5 R at the separation of 1.0 D, but calculated values were smaller by up to 0.06 m/s towards the axis.

The rms of the velocity fluctuations at the exit showed a broad peak at the axis, compatible with that in axial pressure gradient, followed by a minimum at 0.96 R and then a second sharp peak of similar amplitude at the wall at 1.0 R where large velocity gradients led to shear generated turbulence. The calculated rms velocity at the axis, normalized by bulk velocity, remained constant at 20, 14 and 13% with the three models, as the bulk velocity increased from

0.85 to 3.40 m/s at the nozzle separation of 0.4 D while measured values of axial and radial rms were constant at 16 and 10%. This shows that all the models reproduced qualitatively the proportionality between turbulence intensity and bulk velocity but the Jones and Launder model overestimated measured values of both components of rms velocity by up to a factor of two while the alternative models underestimated the axial component and overestimated the radial component by up to 30%. It is possible that the hot-wire measurements involved some rectification effects which would have had the effect of increasing mean and decreasing turbulence results.

Normalized axial rms velocity fluctuations at the exit of nozzles and pipes are shown in Figure 12 together with measured values. The values calculated with the Jones and Launder model increased from 12 to 44% for nozzles and from 16 to 55% for pipes, as the separation was reduced from 2.0 to 0.2 D, while measured values in nozzles increased from 8 to 20%. It is apparent that the qualitative trends are correct but values were overestimated by a factor of 2 by the Jones and Launder model. The RNG and Chen and Kim models produced qualitatively similar profiles of axial rms velocity with calculated values that increased from 11 to 20% with the RNG model and from 11 to 18% with the Chen and Kim model as the nozzle separation was reduced by the same amount and agreement with measurements was, again, within 30% of measured values due to the additional dissipation terms that helped reduce the overestimate.

The integral length scale for all the models had a peak value of around 4 mm at the axis while values were zero at the wall. The values at the axis increased from 2 to 7 mm with the Jones and Launder model, 1 to 6 mm with the RNG model and from 1 to 7 mm with the Chen and Kim model as the nozzle separation increased from 0.2 to 2.0 D. All the models compared well with hot wire measurements by Kostiuk [33] at the separation of 2.0 D that showed the integral length scale was expected to be 4 mm.

Distributions of mean pressure *along the axis* of opposed nozzles had a peak at the stagnation point and decreased to a minimum upstream of the nozzle exit, followed by a small increase towards the inlet boundary. The stagnation pressure was almost directly proportional to U_b^2 with normalized values ranging from 2.80 to 2.18 ρU_b^2 as the bulk velocity increased from 0.85 to 3.40 m/s at the nozzle separation of 0.4 D. The stagnation pressure increased from near zero to 8 ρU_b^2 as the nozzle separation was reduced from 2.0 to 0.2 D at the bulk velocity of 3.3 m/s. Distributions of pressure along the axis of opposed pipes also had a peak at the stagnation point where it was 12% greater than that of the nozzles, and the pressure reduced with distance from the stagnation point towards the inlet boundary.

The normalized axial velocity along the axis of opposed nozzles increased by 16% from the inlet boundary to a peak upstream of the exit, corresponding to the minimum in the distribution of pressure above, followed by a reduction to zero at the stagnation point. The axial velocity, in nozzles and pipes, was almost directly proportional to bulk velocity so that the normalized axial velocity reduced by less than 7% as the bulk velocity was doubled. The absence of a minimum in distributions of pressure in opposed pipes meant that there was no corresponding peak in axial velocity. The axial velocity increased towards the inlet boundary upstream of the pipe exit, where the fully developed boundary condition meant that it was a factor of 1.3 greater than that of the nozzle, and it was zero at stagnation.

The axial strain rate was directly proportional to bulk velocity and increased from 180 to 521/s for nozzles and from 194 to 596/s for pipes as the separation was reduced from 2.0 to 0.2 D at the bulk velocity of 3.3 m/s. Korusoy and Whitelaw [26] confirmed the proportionality

and measured larger values, from 230 to 1320/s, with nozzles. In contrast to laminar flows, reduction in separation resulted in similar increases in strain rate for pipes and nozzles.

The distributions of the rms velocity fluctuations peaked at the stagnation point and were qualitatively similar to those measured by Kostiuk [33]. The rms velocity fluctuations were directly proportional to bulk velocity at all points along the distribution and the proportionality was expected from past measurements. Calculated values of rms at the stagnation point increased little with separation at 55% for nozzles and from 60 to 69% with pipes as the separation was reduced from 2.0 to 0.2 D. Values of axial rms velocity at the stagnation point measured by Kostiuk increased from 12 to 26% while the radial rms increased from 7 to 14% as the nozzle separation was reduced from 2.00 to 0.56 D. This shows that the Jones and Launder model overestimated rms velocities at the stagnation point by up to a factor of 4, as expected from the findings of Dianat *et al.* [18] who suggested the overestimate was a consequence of the inadequacy of the Boussinesq constitutive relation in stagnating turbulence. Both the RNG and Chen and Kim models produced much smaller values of rms that increased from 23 to 24% as the nozzle separation decreased from 2.0 to 0.2 D. The RNG and Chen and Kim models produced results that were closer to measurements than the Jones and Launder model, helped by the addition terms in their dissipation equations, however the quantitative increase in rms velocity at the stagnation plane with decrease in separation was not reproduced correctly with any of the models and Dianat *et al.* [18] suggested that the Boussinesq assumption should be abandoned if better accuracy is to be achieved.

Profiles of pressure on the stagnation plane had a maximum and decreased to that of the surroundings at radii greater than 2.0 R, and the peak broadened with reduction in nozzle separation, as discussed in laminar and inviscid flows. The radial pressure gradients for nozzles and pipes were the same, in contrast to previous differences in laminar flows.

Profiles of radial velocity on the stagnation plane of opposed nozzles with separation 0.4 D, again chosen to match the experiments of Korusoy and Whitelaw [25], increased from zero at the axis to a maximum of 1.7 U_b at 1.4 R, after which entrainment and continuity caused a reduction. The radial velocity was directly proportional to bulk velocity so that the normalized radial velocity was constant to within 1% as the bulk velocity increased from 0.85 to 3.40m/s. Proportionality between bulk and radial velocity was also observed in the LDV measurements of Korusoy and Whitelaw where a slightly higher peak velocity of 1.9 U_b was observed at the same radial position and nozzle separation. Figure 13 allows comparison of calculated profiles of radial velocity in opposed nozzles and pipes together with those measured with nozzles by Korusoy and Whitelaw for a range of separations. The calculated amplitude of the peak increased from 0.56 to 3.37 U_b and moved closer to the axis, from 1.6 to 1.2 R, as the nozzle separation was reduced from 2.0 to 0.2 D. The difference in calculated profiles of pipes and nozzles was less than 1% at separations of less than 0.8 D while the amplitude of the peak was up to 5% greater with nozzles at larger separations. Measured radial velocities agreed with calculations to better than 5% within 1.1 R of the axis. The discrepancy between calculations and measurements increased at larger radii, as discussed in relation to grids, but outside the main range of interest of the results. It is evident from Figure 13 that profiles of radial velocity along the stagnation plane of pipes and nozzles did not differ by more than 5% and this is in contrast to much larger differences discussed above in the laminar flows and due to the greater mixing associated with the turbulent flows.

Continuity required equal axial and radial components of strain rate and those calculated from the profiles of radial velocity in Figure 13 are shown in Figure 14 together with measured

values from Reference [25] with the scale expanded to show the peak at 1.0 R. The calculations showed that the amplitude of the peak increased from 230 to 2642/s as the nozzle separation was reduced from 2.0 to 0.2 D, while the minimum strain rate at the axis increased from 180 to 521/s, at the bulk velocity of 3.3 m/s. The measured and calculated strain rates agree within 5% close to the axis at separations of 0.2 and 0.4 D, but the calculations overestimated the measured values by up to 9% at the separation of 1.0 D. The uncertainties remained less than 10% towards the peak at separations of 0.4 and 1.0 D but the calculated peak strain rate was 20% greater at the smallest separation in Figure 14. The peak strain rate for pipes and nozzles was the same for all the separations considered while the value at the axis of pipes was greater than that of nozzles, by up to 12% at the smallest separation of 0.2 D. The difference between pipes and nozzles decreased with increased separation until the strain rates at the axis were near equal at 2.0 D. The strain rates are summarized in Table V.

The Jones and Launder model resulted in rms velocity fluctuations at the stagnation plane that were directly proportional to bulk velocity and had a value of 0.6 U_b at the axis at the separation of 0.4 D and increased to a peak value of 0.7 U_b at 1.0 R, after which there was a reduction. Profiles of normalized rms velocity fluctuations are presented in Figure 15 for a range of separations from 0.2 to 2.0 D. The peaks are evident at 1.0 R with separations of 0.2 and 0.4 D where the values of rms increased from 55 to 120% as the separation of opposed nozzles decreased from 2.0 to 0.2 D. The measurements of radial rms velocities from Korusoy and Whitelaw [25] confirmed the increase with a reduction in nozzle separation but the values at the axis ranged 10–30% as the separation reduced from 1.0 to 0.4 D and were smaller than calculated values. The measurements also confirmed that there was a peak in the rms profiles at separations of 0.2 and 0.4 D but not at 1.0 D while the position of the peak was slightly closer to the axis, at 0.84 R, than the calculated position of 1.0 R. The figure indicates that rms values for pipes and nozzles were within 3%.

The Chen and Kim model produced rms values, Figure 16, that agree with measurements to within 5% and increased from 20 to 25% at the axis while the increase at the peak at 1.0 R was from 20 to 40%. Comparison of the model equations in Section 2 shows that they are equivalent in the limit of zero strain rate and this explains why they overestimated the measurements by similar factors at large separations. The Chen and Kim and RNG models have additional terms in their dissipation equations that are fourth order in strain rate so that the dissipation increased more rapidly with reduction in separation than with the Jones and Launder model. These additional terms were effective at keeping the turbulence intensity within realistic limits in regions of stagnation and high curvature but led to an underestimate of rms velocities at small separations.

The turbulent strain rate is expected to be high when the rms of the velocity fluctuations is high and estimates based of the velocity gradient and the numbers in the previous paragraph show that the peak of the rms strain rate fluctuations was at 1.0 R and was directly proportional to bulk velocity with a value of 184/s at the bulk velocity of 3.3 m/s and nozzle separation 0.4 D. The calculations also suggest that the rms of the strain rate fluctuations at the peak increased from 146 to 292/s, as the nozzle separation was reduced from 2.0 to 0.2 D.

5. CONCLUSIONS

Calculations of isothermal inviscid, laminar and turbulent flows were performed successfully with a desktop computer in conjunction with commercially available software and QUICK

differencing. The use of higher order schemes required the development of an optimized grid and was otherwise prohibitively expensive because of the need for small Peclet numbers. Uncertainties due to numerical diffusion were expected at the exit near the wall where the flow curvature and velocity was greatest. Preliminary calculations quantified suitable positions for the pressure and inlet boundaries and showed that the latter must be applied more than 1.0 D upstream of the nozzle or pipe exit.

The inviscid flow calculations reproduced qualitatively the non-uniform exit velocity profile of the experiments at small separations and overestimated the peak in axial velocity by 30% leading to an overestimate of the peak in the profile of mean strain rate at the stagnation plane of 11%. The strain rates at the axis and peak of the distribution at the stagnation plane are summarized in Tables III and IV as a function of separation for inviscid, laminar and turbulent flows with pipe and nozzle boundary conditions.

The existence of peaks in strain rate at 1.0 R at small nozzle separations and with laminar flow, suggests that local quenching of reacting flows should occur initially in their vicinity with growth of the quenched region towards the axis as the bulk velocity was increased to complete extinction. As expected the strain rate increased with Reynolds number and with reduction in separation. The main difference between pipes and nozzles was the additional peak in strain rate on the axis of pipes that implies that extinction should occur from large to small radii with small separations and the opposite at larger separations. The strain rate at the stagnation point was overestimated by the bulk strain rate, $2U_b/H$, by up to a factor of 5 for nozzles and 2 for pipes.

Measured profiles of strain rate at the stagnation plane were reproduced by the turbulent nozzle flow calculations to within 10% and extended to show that differences between pipes and nozzles were smaller in turbulent than laminar flows. In both cases, the strain rate peaked close to 1.0 R, with a minimum at the axis and slightly higher values with pipes. The increasing amplitude of the peak in strain rate at small nozzle separations explained the occurrence of local quenching in the experiments of Korusoy and Whitelaw [26] and the similarity with pipes suggests that local quenching should also be observed in pipe flows. The slightly higher mean strain rate in pipe flows suggests that extinction in pipes should occur at lower bulk velocities than nozzles. The maximum strain rates are summarized in Table V.

The Jones and Launder model overestimated the rms velocity fluctuations at the stagnation plane by a factor of up to 4 while the renormalization group and Chen and Kim models led to similar overestimation at separations greater than 0.8 D, where strain rates were low and the models were equivalent. The renormalization group and Chen and Kim models underestimated rms velocities by up to 20% at the separation of 0.2 D, where strain rates were high, because of the additional production terms in the dissipation equation that were to fourth order in the strain rate. This means that the first-moment closures used here are unlikely to be appropriate for extinction and relight calculations because they could not represent the rms of the strain rate fluctuations. A model with production terms in both k and ε equations may produce better results, however turbulence and its effects are anisotropic in the stagnation plane of opposed flows and this implies that the Boussinesq constitutive relation and the gradient diffusion approximations will lead to inaccuracies in numerical simulations of this region.

ACKNOWLEDGEMENTS

We are grateful to the United States Office of Naval Research, which supported this work under contracts N00014-99-1-0832 and N00014-02-1-0664. Many useful discussions with Profs H McDonald, WP Jones

and RT Fenner are gratefully acknowledged and we are pleased to thank Dr F Nadiri and Dr D Barnes for practical assistance with hardware and software.

REFERENCES

1. Chelliah HK, Law CK, Ueda T, Smooke MD, Williams FA. An experimental and theoretical investigation of the dilution, pressure, and flow-field effects on the extinction condition of methane–air–nitrogen diffusion flames. In *Proceedings of 23rd International Symposium on Combustion*, Pittsburgh, 1990; 503–511.
2. Konnov AA, Idir M, Delfau JL, Vovelle C. Experimental study of extinction of nonadiabatic counterflow premixed flames. *Combustion and Flame* 1996; **105**:308–320.
3. Pellet GL, Isaac KM, Humphreys Jr WM, Gartrell LR, Roberts WL, Dancey CL, Northam GB. Velocity and thermal structure, and strain-induced extinction of 14 to 100% hydrogen–air counterflow diffusion flames. *Combustion and Flame* 1998; **112**:575–592.
4. Mastorakos N. Turbulent combustion in opposed jet flows. *Ph.D. Thesis*, Imperial College London, U.K., 1993.
5. Sardi E. Turbulent flame extinction in unforced and periodically forced counterflows. *Ph.D. Thesis*, Imperial College London, U.K., 1997.
6. Korusoy E. Opposed jets, flames and extinction. *Ph.D. Thesis*, Imperial College London, U.K., 2002.
7. Hamins A, Trees D, Seshadri K, Chelliah HK. Extinction of nonpremixed flames with halogenated fire suppressants. *Combustion and Flame* 1994; **99**:221–230.
8. Fallon GS, Chelliah HK, Linteris GT. Chemical effects of CF3H in extinguishing counterflow CO/Air/H2 diffusion flames. In *Proceedings of 26th International Symposium on Combustion*, Pittsburgh, 1996; 1395–1403.
9. Gao LP, D'Angelo Y, Silverman I, Gomez A, Smooke MD. Quantitative comparison of detailed numerical computations and experiments in counterflow spray diffusion flames. In *Proceedings of 26th International Symposium on Combustion*, Pittsburgh, 1996; 1739–1746.
10. Frouzakis CE, Lee J, Tomboulides AG, Boulouchos K. Two-dimensional direct numerical simulation of opposed-jet hydrogen–air diffusion flame. In *Proceedings of the 27th International Symposium on Combustion*, Pittsburgh, 1998; 571–577.
11. Massot M, Manoj K, Smooke MD, Gomez A. Spray counterflow diffusion flames of heptane: experiments and computations with detailed kinetics and transport. In *Proceedings of the 27th International Symposium on Combustion*, Pittsburgh, 1998; 1975–1983.
12. Sung CJ, Law CK, Chen J-Y. An augmented reduced mechanism for methane oxidation with comprehensive global parametric validation. In *Proceedings of the 27th International Symposium on Combustion*, Pittsburgh, 1998; 295–304.
13. Lahjaily H, Champion D, Karmed D, Bruel P. Introduction to dilution in the BML model: application to a stagnating turbulent flame. *Combustion Science and Technology* 1998; **135**:153–173.
14. Zegers EJP, Williams BA, Fisher EM, Fleming JW, Sheinson RS. Suppression of nonpremixed flames by fluorinated ethanes and propanes. *Combustion and Flame* 2000; **121**:471–487.
15. Jones WP, Launder BE. The prediction of laminarization with a two-equation model of turbulence. *International Journal of Heat and Mass Transfer* 1972; **15**:301–314.
16. Launder BE, Sharma BI. Application of the energy-dissipation model of turbulence to the calculation of flow near a spinning disc. *Letters in Heat and Mass Transfer* 1974; **1**:131–138.
17. Craft TJ, Graham LJW, Launder BE. Impinging jet studies for turbulence model assessment—II. An examination of the performance of four turbulence models. *International Journal of Heat and Mass Transfer* 1993; **36**: 2685–2697.
18. Dianat M, Fairweather M, Jones WP. Predictions of axisymmetric and two-dimensional impinging turbulent jets. *International Journal of Heat and Fluid Flow* 1996; **17**:530–538.
19. Jones WP, Prasetyo Y. Probability density function modelling of premixed turbulent opposed jet flames. In *Proceedings of the 27th International Symposium on Combustion*, Pittsburgh, 1996; 275–282.
20. Champion M, Libby PA. Stagnation streamline turbulence revisited. *AIAA Journal* 1990; **28**:1525–1526.
21. Champion M, Libby PA. Asymptotic analysis of stagnating turbulent flows. *AIAA Journal* 1991; **29**:16–24.
22. Champion M, Libby PA. Reynolds stress description of opposed and impinging turbulent jets; Part I: closely spaced opposed jets. *Physics of Fluids* 1993; **5**:203–216.
23. Champion M, Libby PA. Reynolds stress description of opposed and impinging turbulent jets. II. Axisymmetric jets impinging on nearby walls. *Physics of Fluids* 1994; **6**:1805–1819.
24. Lindstedt RP, Váos EM. Modelling of premixed turbulent flames with second moment methods. *Combustion and Flame* 1999; **116**:461–485.
25. Korusoy E, Whitelaw JH. Opposed jets with small separations and their implications for the extinction of opposed flames. *Experiments in Fluids* 2001; **31**:111–117.
26. Korusoy E, Whitelaw JH. Extinction and relight in opposed flames. *Experiments in Fluids* 2002; **33**:75–89.

27. Leclerc A. Déviation d'un jet liquide par une plaque normale à son axe. *La Houille Blanche* 1950; **6**:3–8.
28. Spalding DB. Theory of mixing and chemical reaction in the opposed-jet diffusion flame. *Journal of the American Rocket Society* 1961; **3**:763–771.
29. Tsuji H. Counterflow diffusion flames. *Progress in Energy and Combustion Science* 1982; **8**:93–119.
30. Seshadri K, Williams FA. Laminar flow between parallel plates with injection of a reactant at high Reynolds number. *International Journal of Heat and Mass Transfer* 1978; **21**:251–253.
31. Rolon JC, Veynante D, Martin JP, Durst F. Counter jet stagnation flows. *Experiments in Fluids* 1991; **11**: 313–324.
32. Kostiuk LW, Bray KNC, Cheng RK. Experimental study of premixed turbulent combustion in opposed streams. Part I—Nonreacting flow field. *Combustion and Flame* 1993; **92**:377–395.
33. Kostiuk LW. Premixed turbulent combustion in counterflowing streams. *Ph.D. Thesis*, Churchill College, University of Cambridge, U.K., 1991.
34. Pope SB. *Turbulent Flows*. Cambridge University Press: Cambridge, U.K., 2000.
35. Cebeci T, Smith AMO. Analysis of turbulent boundary layers. *Applied Mathematics and Mechanics*, vol. 15. Academic Press: New York, 1974.
36. Baldwin BS, Lomax H. Thin layer approximation and algebraic model for separated turbulent flow. *AIAA Paper* 78-257, 1978.
37. Rodi W. *Turbulence Models and their Application in Hydraulics—A State of the Art Review*. IAHR: Delft, The Netherlands, 1980.
38. Cooper D, Jackson DC, Launder BE, Liao GX. Impinging jet studies for turbulence model assessment—I. Flow-field experiments. *International Journal of Heat and Mass Transfer* 1993; **36**:2675–2684.
39. Craft TJ, Launder BE, Suga K. Development and application of a cubic eddy-viscosity model of turbulence. *International Journal of Heat and Fluid Flow* 1996; **17**:108–115.
40. Jones WP. Personal communication, 2002.
41. Jones WP, Whitelaw JH. Calculation methods for reacting turbulent flows: a review. *Combustion and Flame* 1982; **48**:1–26.
42. Bray KNC. Challenge of turbulent combustion. *Proceedings of the 26th International Symposium on Combustion*, Pittsburgh, 1996; **1**:1–26.
43. Bray KNC, Champion M, Libby PA. Premixed flames in stagnating turbulence. Part I. The general formulation for counterflowing streams and gradient models for turbulent transport. *Combustion and Flame* 1991; **84**: 391–410.
44. Bray KNC, Champion M, Libby PA. Premixed flames in stagnating turbulence. Part III. The turbulent kinetic energy and mean viscous dissipation (Kappa–Epsilon) theory for reactants impinging on a wall. *Combustion and Flame* 1992; **91**:165–186.
45. Bray KNC, Champion M, Libby PA. Premixed flames in stagnating turbulence. Part IV. A new theory for the Reynolds stresses and Reynolds fluxes applied to impinging flows. *Combustion and Flame* 2000; **120**:1–18.
46. Bray KNC, Champion M, Libby PA. Premixed flames in stagnating turbulence. Part V. Evaluation of models for the chemical source term. *Combustion and Flame* 2001; **127**:2023–2040.
47. Chen YS, Kim SW. Computation of turbulent flows using an extended k–ε turbulence closure model. *NASA CR*-179204, 1987.
48. Yakhot V, Orszag SA. Renormalisation group analysis of turbulence—I: basic theory. *Journal of Scientific Computing* 1986; **1**:1–51.
49. El Tahry SH. K–ε Equation for compressible reciprocating engine flows. *AIAA Journal of Energy* 1983; **7**(4):345–353.
50. Yakhot V, Orszag SA, Thangam S, Gatski TB, Speziale CG. Development of turbulence models for shear flows by a double expansion technique. *Physics of Fluids* 1992; **A4**(7):1510–1520.
51. Versteeg HK, Malalasekera W. *An Introduction to Computational Fluid Dynamics: the Finite Volume Method*. Prentice-Hall, International: Englewood Cliffs, NJ, 1995.
52. Patankar SV. *Numerical Heat Transfer and Fluid Flow*. Hemisphere: Washington, DC, 1980.
53. Ferziger JH, Peric M. *Computational Methods for Fluid Dynamics*. Springer: Berlin, London, 1996.
54. Kershaw DS. The incomplete Cholesky conjugate gradient method for iterative solution of linear equations. *Journal of Computational Physics* 1978; **26**:43–65.
55. de Vahl Davis G, Mallinson GD. False diffusion in numerical fluid mechanics. *Report Number* 1972/FMT/1, School of Mechanical and Industrial Engineering, University of New South Wales, Australia, 1972.

